Miner Deposita (2011) 46:319–335
DOI 10.1007/s00126-011-0334-y

ARTICLE

Discriminant diagrams for iron oxide trace element fingerprinting of mineral deposit types

Céline Dupuis · Georges Beaudoin

Received: 10 February 2010 / Accepted: 11 January 2011 / Published online: 8 February 2011

Abstract Magnetite and hematite are common minerals in a range of mineral deposit types. These minerals form partial to complete solid solutions with magnetite, chromite, and spinel series, and ulvospinel as a result of divalent, trivalent, and tetravalent cation substitutions. Electron microprobe analyses of minor and trace elements in magnetite and hematite from a range of mineral deposit types (iron oxide-copper-gold (IOCG), Kiruna apatite–magnetite, banded iron formation (BIF), porphyry Cu, Fe-Cu skarn, Fe-Ti, V, Cr, Ni-Cu-PGE, Cu-Zn-Pb volcanogenic massive sulfide (VMS) and Archean Au-Cu porphyry and Opemiska Cu veins) show compositional differences that can be related to deposit types, and are used to construct discriminant diagrams that separate different styles of mineralization. The Ni+Cr vs. Si+Mg diagram can be used to isolate Ni-Cu-PGE, and Cr deposits from other deposit types. Similarly, the Al/(Zn+Ca) vs. Cu/(Si+Ca) diagram can be used to separate Cu-Zn-Pb VMS deposits from other deposit types. Samples plotting outside the Ni-Cu-PGE and Cu-Zn-Pb VMS fields are discriminated using the Ni/(Cr+Mn) vs. Ti+V or Ca+Al+Mn vs. Ti+V diagrams that discriminate for IOCG, Kiruna, porphyry Cu, BIF, skarn, Fe-Ti, and V deposits.

Keywords Magnetite · Hematite · Mineral deposit · Electron microprobe · Mineral chemistry · Discriminant diagram

Editorial handling: T. Wagner

C. Dupuis · G. Beaudoin (✉)
Département de géologie et de génie géologique,
Université Laval,
Québec (QC) G1V 0A6, Canada
e-mail: beaudoin@ggl.ulaval.ca

Introduction

Magnetite and hematite are two common oxide minerals in magmatic, sedimentary, and metamorphic rocks (e.g., Ramdohr 1980; Scheka et al. 1980) and can be major to trace minerals in a range of mineral deposit types. Magnetite occurs typically as an accessory mineral in many igneous rocks, but is locally concentrated by magmatic segregation or by crystal settling, forming magnetite-rich bands (Deer et al. 1992). Metamorphism is known to yield compositionally homogeneous, low-Ti magnetite (Hall and Fischer 1977; Johnson 1979), and metasomatic reactions in metamorphosed volcanogenic massive sulfide (VMS) deposits yields gahnite in equilibrium with its host rocks (Heimann et al. 2005). In addition to forming iron ore in various types of sedimentary ironstones, iron oxides are abundant in iron oxide-copper-gold (IOCG) and Kiruna-type apatite–magnetite, Fe-Ti, and in various types of porphyry and skarn deposits. Iron oxides also form minor to trace minerals in a large number of deposit types, including Ni-Cu-PGE magmatic massive sulfides, Cu-Zn-Pb VMS, Opemiska-type Cu veins and clastic-dominated Pb-Zn deposits (Leach et al. 2010). Variations in the whole rock chemical environment in which magnetite grows control its chemical composition (Hutton 1950; Buddington and Lindsley 1964; Scheka et al. 1980; Razjigaeva and Naumova 1992; Deer et al. 1992). Consequently, the range in physico-chemical conditions during formation in various mineral deposit environments probably controls the chemical composition of iron oxides in mineral deposits, such that this compositional variety can possibly be used to fingerprint mineral deposit types (Carew 2004; Gosselin et al. 2006; Singoyi et al. 2006; Beaudoin et al. 2007).

In detrital sedimentary rocks, iron oxides are the most common heavy minerals (Pettijohn et al. 1987). Razjigaeva

and Naumova (1992) showed that Ti, Mn, Cr, V, Ni, Co, Zr, Sn, Zn, Pb, and Cu concentration could be used to trace the source rocks of sediments whereas Grigsby (1990) used a combination of petrographic exsolution features and chemical composition criteria in a flowchart decision tree to determine the likely source of detrital magnetite grains. Apatite is another mineral that has been shown to have chemical composition characteristic of its formation environment (Belousova et al. 2002), which has been used for detrital sediment provenance studies (Morton and Yaxley 2007).

The use of iron oxide mineral chemistry to fingerprint mineral deposits is not unlike the well-known use of spinel in petrogenetic studies (Barnes and Roeder 2001), as well as the use of indicator minerals for diamond exploration (Fipke et al. 1995). Terrestrial spinel shows a wide range in composition that records different magmatic histories and metamorphic reequilibration. In addition, major and minor element composition of spinel records processes of high to low pressure crystallization and crustal contamination (Barnes and Roeder 2001). Using contoured data density plots of about 26,000 spinels, Barnes and Roeder (2001) were able to outline fields typical of various mafic–ultramafic rocks. The zincian spinel gahnite is a common accessory mineral in amphibolite to granulite metamorphic zinc-bearing rocks rich in sulfides (Spry and Scott 1986; Heimann et al. 2005), and can be used as an exploration tool for metamorphosed VMS deposits (Spry and Scott 1986; Heimann et al. 2005) and Broken Hill-type Ag-Pb-Zn deposits (Walters et al. 2002). Zincian spinel composition depends not only on the chemical composition of the rocks, but also on the temperature of metamorphic equilibrium (Heimann et al. 2005).

Carew (2004) used the laser ablation inductively coupled plasma mass spectrometry (LA-ICP-MS) technique to measure a large range of trace elements in magnetite, hematite, pyrite, and chalcopyrite from IOCG deposits, Na-Ca and K-Fe alteration, barren ironstones, and hostrocks from the Cloncurry district in Australia. In hematite, Carew (2004) found that Ti, Si, Mg, Al, Co, Ni, As, Sn, Sb, Zr, V, Mn, W, Sc, Ga, and Nb were all detected whereas La, Mo, Ce, In, Hf, Bi, Pb, U, and Cu were commonly close or below detection limit. In magnetite, Carew (2004) found that Ti, Si, Al, Mg, V, Cr, Mn, Co, Ni, Cu, Zn, Ga, Sn, and Pb were commonly above detection limit whereas As, Zr, Y, U, Hf, La, Ce, Bi, Sb, In, Mo, W, and Sn had lower concentration commonly near or below detection limit. According to Carew (2004), trace element patterns for Kiruna-type deposits from Sweden and Chile are different from those of Cloncurry district IOCG mineralization. In addition, Carew (2004) showed that magnetite from the Osborne deposit has a different trace element composition compared to that of the Ernest Henry IOCG deposit. In summary, Carew (2004) showed that magnetite from Cloncurry district IOCG deposits is characterized by higher Sn and Mn and lower V, Ti, Mg, Si, Cr, and Zn concentrations compared to barren ironstones whereas hematite is characterized by higher As, Ga, Sb, and W concentration. Rusk et al. (2009) also used the LA-ICP-MS to measure trace elements in magnetite from unmineralized hydrothermal breccias from the Cloncurry region. Rusk et al. (2009) observed that magnetite from barren breccias is enriched in V and depleted in Mn relative to ore-related magnetite from Ernest Henry, and concluded that the difference in magnetite chemistry probably results from mineral equilibrium at the site of magnetite deposition.

Singoyi et al. (2006) measured the trace element composition of magnetite from selected VMS, skarn, IOCG, and Broken Hill-type clastic-dominated Pb-Zn deposits from Australia, and divided the data into three groups: group A elements (Mg, Al, Ti, V, Mn, Co, Ni, Zn, Ga, Sn) are commonly measured above the detection limit using LA-ICP-MS and have consistent results and elemental patterns from grain to grain in one sample, group B elements (Cr, As, Zr, Nb, Mo, REE, Ta, W, Pb) yielded lower and heterogeneous concentration and patterns, whereas group C elements (Cu, Ag, Se, Tl, Te, Bi, Au) were commonly below the minimum limit of detection. Singoyi et al. (2006) showed that the Sn/Ga vs. Al/Co diagram has potential to distinguish the deposit types that they studied. Finally, Nadoll et al. (2009) measured trace elements in magnetite from hydrothermal ore deposits and their host rocks in the Proterozoic Belt Supergroup of western Montana and northern Idaho (USA) using both electron microprobe (EMPA) and LA-ICP-MS methods. Factor analysis reveals small but distinct differences between magnetite from the various geological settings that define magnetite varieties: (1) magnetite with elevated Mg-Mn from hydrothermal Ag-Pb-Zn veins and post-metamorphic igneous intrusions, and (2) magnetite with elevated V-Co-Zn from burial metamorphic rocks, post-metamorphic igneous intrusions and sediment-hosted Cu-Ag deposits. According to Nadoll et al. (2009), the fact that only subtle geochemical differences were observed can be explained by the low temperature of formation of the orebodies and the metamorphic history of the Belt terrane, resulting in sub-solidus re-equilibration of hydrothermal magnetite.

Mineralogy of the spinel group

The spinel group minerals have the general formula XY_2O_4, where X is divalent (2+) and Y is trivalent (3+), and it displays a wide range of chemical composition (Fig. 1) owing to several solid solution substitutions of divalent and trivalent cations (Deer et al. 1992). Spinel is

used as a petrogenetic mineral because its chemical composition is controlled by the environment in which it forms (Barnes and Roeder 2001). Zincian spinel gahnite in metamorphic VMS deposits also displays a chemistry largely controlled by the chemistry of the metamorphic host rocks (Heimann et al. 2005).

The spinel group minerals are divided in three series according to the trivalent cation (Fig. 1): the spinel series (Al^{3+}), the magnetite series (Fe^{3+}), and the chromite series (Cr^{3+}). In the "magnetite series", magnetite ($Fe^{2+}Fe_2^{3+}O_4$) forms a complete solid solution with magnesioferrite ($MgFe_2O_4$) and ulvöspinel (Fe_2TiO_4), also known as titanomagnetite (Deer et al. 1992). Temperature-dependent exchange of $Fe^{2+}+Ti^{4+}$ for 2 Fe^{3+} between titanomagnetite and the ilmenite–hematite solid solution, and iron redox equilibrium between magnetite, ilmenite, and ulvöspinel, are the basis for the Fe-Ti thermo-oxybarometer (Buddington and Lindsley 1964; Sauerzapf et al. 2008). Magnetite displays partial solid solutions with franklinite ($ZnFe_2O_4$), jacobsite ($MnFe_2O_4$), and trevorite ($NiFe_2O_4$). Vanadium (V^{3+}), calcium (Ca^{2+}), and cobalt (Co^{2+}) are also known to substitute widely in the magnetite structure. Complete solid solution of the trivalent cation (Cr^{3+}) with chromite ($FeCr_2O_4$) and magnesiochromite ($MgCr_2O_4$) forms the "chromite series". Of the four "spinel series" end-members spinel sensu stricto ($MgAl_2O_4$), hercynite ($FeAl_2O_4$), gahnite ($ZnAl_2O_4$) and galaxite ($MnAl_2O_4$), magnetite displays partial solid solution with hercynite only.

Hematite (Fe_2O_3) forms a complete solid solution with ilmenite ($FeTiO_3$) at high temperature (above 1,050°C), and limited solid solution with magnetite (Fe_3O_4), corundum (Al_2O_3), and bixbyite (Mn_2O_3; Deer et al. 1992). Hematite replacement of magnetite is termed "martite" whereas replacement of hematite by magnetite is widely referred to as "mushketovite".

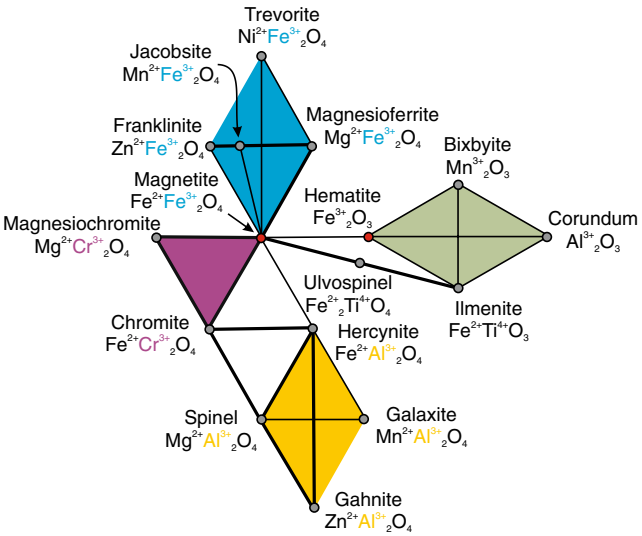

Fig. 1 Schematic representation of the spinel group minerals with complete solid solution shown by *thick lines* and partial solid solution represented as *thin lines* between minerals

Analytical method

Electron microprobe analyses

Polished thin sections were analyzed using the Université Laval CAMECA SX-100 electron microprobe, equipped with five wavelength-dispersive spectrometers, under a 10-μm diameter beam with a voltage of 15 kV and a current of 100 nA. The wide beam diameter is necessary to prevent overheating of magnetite and hematite grains under the high current conditions. Analytical conditions are shown in Table 1. The analyses were calibrated using a range of natural and synthetic standards, comprising simple oxides (GEO Standard Block of P and H Developments), or minerals (Mineral Standard Mount MINM 25–53, Astimex Scientific; Jarosewich et al. 1980). After counting over the peak for 20–30 s, background was measured on one side of the peak for 10 s at an offset position in a flat region of the spectrum experimentally verified to be free of interfering element X-ray wavelengths (Table 1). Determination of *V* concentration using the Kα line is affected by interference from the adjacent Ti Kβ line, but this interference is minor at low Ti concentrations. These settings yielded minimum detection limits (C_{min}) as low as ~20–30 ppm for elements such as K, Ca, Al, Si, Ti, and Mg; ~50–90 ppm for Mn, Cr, and V; ~200–500 ppm for Cu, Zn, and Ni (Table 1). The minimum detection limit was computed for each element in each analysis by the CAMECA software using the formula of Ancey et al. (1978):

$$C_{\min} = \left(\frac{FC_t}{I_t - B_t}\right) \times \left(\frac{\lambda(\alpha,\beta)}{2t_e}\sqrt{1 + \frac{4B_e t_e\left(1+\alpha_e^{-1}\right)}{\lambda(\alpha,\beta)}}\right)$$

where F is a computed correction factor, C_t is the concentration in the standard, I_t is the peak intensity in the standard, B_t is the background intensity in the standard, B_e is the background intensity in the sample, t_e is the counting time for the peak in the sample, α_e is a constant that takes into account the differences in counting times for peak and background, and $\lambda(\alpha,\beta)$ is a tabulated statistical parameter for $\alpha=\beta=5\%$. The optimized analytical routine allows analysis of one spot in less than 5 min.

Although we initially measured the chemical composition for 24 elements (Gosselin et al. 2006), we found that only 12 elements (K, Ca, Al, Si, Ti, Mg, Mn, Cr, V, Cu, Zn, Ni) have average concentration (x) commonly above their minimum detection limit, with $x/C_{min}>1.2$, and concentration variability with a relative standard deviation (s) where $s/x>0.15$ to

Table 1 Analytical conditions for microprobe analysis

Element	Crystal	Line	Sinθ[a]		Counting time (s)		Range of detection limits (ppm)
			Peak	Background	Peak	Background	
Zn	LIF	Kα	0.35635	0.35135	20	10	183–247
Cu	LIF	Kα	0.38256	0.37756	30	10	325–473
Ni	LIF	Kα	0.41173	0.40673	20	10	181–257
Mn	LLIF	Kα	0.52207	0.51607	20	10	52–83
Cr	LLIF	Kα	0.52207	0.51607	20	10	37–63
V	LLIF	Kα	0.62197	0.62797	20	10	41–69
K	LPET	Kα	0.42742	0.42142	20	10	18–21
Ca	LPET	Kα	0.38387	0.37787	20	10	18–23
Ti	LPET	Kα	0.31423	0.30823	20	10	22–30
Al	TAP	Kα	0.32462	0.33062	30	10	19–21
Si	TAP	Kα	0.27737	0.28337	30	10	20–24
Mg	TAP	Kα	0.38502	0.39102	30	10	23–27

[a] $\lambda=2d\ \mathrm{Sin}\theta$, where λ is the wavelength and d is the interplanar distance of the analyzing crystal

allow for efficient use as discriminant elements. The low concentration of several elements such as Au, Sb, Mo, Th, Ba, Co, Y, and Zr does not allow accurate measurement using the electron microprobe, such that other analytical methods such as LA-ICP-MS or PIXE would need to be used for accurate analysis.

Nonparametric distribution modeling to estimate average composition

Electron microprobe datasets are typically censored because they contain non-detects that are below the computed minimum detection limits (Helsel 2005). Data analysis procedures for censored datasets are divided into three classes (Helsel 2005): (1) simple substitution methods, (2) parametric methods, and (3) nonparametric methods. Simple, arbitrary, substitution is the simplest, most often used, method but it is also the least recommended method because it biases estimates depending on the substitution value chosen. Parametric methods require sufficient data to validate the use of a specific population distributional model, whereas nonparametric methods are particularly useful for restricted geochemical datasets because they do not require the assumption of a population distribution type. We use the standard nonparametric Kaplan–Meier (K–M) method to estimate the summary statistics of our censored dataset (Lee and Helsel 2007).

Sample selection

Representative samples from 111 mineral deposits ascribed to 13 deposit types have been investigated (Table 2): (1) IOCG, (2) Kiruna apatite–magnetite, (3) banded iron formation (BIF); (4) porphyry Cu, (5) Archean Au-Cu porphyry, (6) Archean Opemiska-type Cu veins, (7) Fe-Cu-Zn-Pb skarns, (8) Ni-Cu-PGE massive sulfides, (9) Cu-Zn VMS, (10) clastic-dominated Pb-Zn, (11) Cr, (12) Fe-Ti, and (13) V deposits. IOCG deposits commonly have a space–time association, and share certain characteristics, with Kiruna apatite–magnetite deposits, but the latter are not IOCG deposits sensu stricto according to Williams et al. (2005). Other deposits, rich in iron oxides, but of less-well established, or controversial, affiliation are not used to define mineral deposit type chemical composition characteristics in this study, and, therefore, are grouped into a class of "Other hydrothermal iron oxide" deposits which composition is only compared to better established examples (Table 2). An example of this group is the Bayan Obo Fe-REE-Nb deposit, Inner Mongolia, China, which consists of multistage mineralisation with similarities to both the broad group of Fe-oxide-(Cu-U-Au-REE) deposits (Hitzman et al. 1992) and carbonatitic deposits (Smith 2007). Porphyry Cu deposits form a well-established mineral deposit class (Sillitoe 2010) that have yet to be studied according to accepted subtypes and are herein discussed as a single group. Archean Au-Cu deposits with characteristics similar to Phanerozoic porphyry Cu deposits are referred to as Archean Au-Cu porphyries (Fraser 1993). Because recognition of Archean porphyry deposits is commonly hindered by deformation and metamorphism (Griffis 1979), we elected to separate Archean Au-Cu porphyry deposits from well-established Cu porphyry deposits. Opemiska-type Cu veins comprise sulfide–quartz veins found in the Chibougamau–Chapais region, Abitibi greenstone belt, Québec, Canada (Pilote and Guha 1998). They contain Au, Ag, Cu, and Zn and have several characteristics similar with those of

Table 2 List of deposits studied, with number of magnetite (Mt) and hematite (Hm) analyses for each deposit

Type	Deposit name	Analyzes		Type	Deposit Name	Analyses	
		Mt	Hm			Mt	Hm
IOCG	Olympic Dam		18	Skarn	Iron Hill	4	
	Ernest Henry	12			Klanch Hill	6	
	Candelaria	6			Chandman Uul	6	
	Alemao	5			Oyut Ovo	4	
	Kwyjibo	18			Yacumina	8	
	Mont-de-l'Aigle	14	6		Yantac	17	
	Guelb Moghrein	22			Toromocho	8	
	Nico	8	8		Morococha-Surface	9	
	Punta del Cobre	44	27		Jaima	26	11
	Palabora	18			Codiciada-Manto Italia	31	
Other hydrothermal	Queylus	21	1		Phukham	32	35
iron oxide deposits	Osborne	12			Khao Lek	16	
	Fort Constantine	6	4		Singto	8	
	Murdie Island	11	27		PUT1	32	
	San Fernando	6			PUT2	21	21
	Amargosa	6		Ni-Cu	Blue Lake	6	
	Bayan Obo	6			Voisey's Bay	10	
	Marcona	16			Katinniq1	7	
Kiruna-type	Pea Ridge	6	4		Katinniq2	8	
	Pilot Knob	6	2		Mesamax	8	
	Kiruna	5			Expo	8	
	El Romeral	6			Pipe	3	
	Rektor	6	4		Craig	6	
	Savage River	8			McCready East	44	
	El Laco	15	25		Levack	24	
BIF	Schefferville	10	12		Norman	14	
	Richelieu mine	2	5		Whistle	10	
	Spruce Pit		8		Victor	8	
	Pipe	8			Murray	8	
Cu porphyry	Copper Mountain	6			Creighton	8	
	Bingham Canyon	6		VMS	Ansil	22	
	Skouries	11	4		Aldermac	3	
	Ridgeway	6			Normétal	4	
	Oyu Tolgoi	6			Persévérance	8	
	Khargmatai	7			Bell Allard	8	
	Escondida Norte	8	8		Scott	8	
	Sari Gunay	13	6		Bent Hill	8	
	Porgera (deep veins)	8			ODP Mound	20	
	Morococha	18	12		Caribou	53	
	Bajo de la Alumbrera	22	12		Windy Craggy	101	
	Rosia Poieni	4	4		GP4F	10	
	Reko Diq	41	60		Kudz Ze Kayah	28	
Archean	Lamothe #1	8			Boliden	16	
Porphyry	Queylus	8			Garpenberg	12	
	Inlet #3	8			Ducktown	18	
	Corner Bay	8			Fornas	8	

Table 2 (continued)

Type	Deposit name	Analyzes		Type	Deposit Name	Analyses	
		Mt	Hm			Mt	Hm
Opemiska	Portage	8			Besshi	5	
Cu veins	Copper Cliff	8		Clastic Pb-Zn	Faro-Vangorda	16	
	Merrill	8			Broken Hill		10
	Springer	8		Fe-Ti	GE mine	8	
	Lessard	8			La Blache	4	
	Brosman	10			Sudbury-Ti	6	
	Lac Ham	7			Girardville	15	
	Copper Rand	6			Routivare	16	
Cr	Coleraine	3		V	Lac Doré	5	

Archean Au-Cu porphyry deposits in the Chibougamau–Chapais area. VMS deposits also have yet to be studied according to accepted subtypes (Franklin et al. 2005) and are herein discussed as a single group.

For each deposit studied, between one and ten polished sections or polished thin sections sampled from ore zones have been used, from which three to four magnetite and/or hematite grains have been analyzed by at least two spots per grain with the electron microprobe. The number of magnetite and hematite analyses for each deposit is listed in Table 2. Analyses with more than 2 wt.% of the elements listed in Table 1 were not used to compute deposit average composition, with the exception of Cr, Ti, and V for Cr, Fe-Ti, and V deposits, respectively, which have high concentrations in iron oxides from these deposits. The chemical composition of iron oxides discussed below is based on nearly 2,000 individual analyses.

Iron oxide composition of selected deposit types

The average composition of magnetite and/or hematite from several deposit types is described using the average composition from all spot analyses from one deposit, estimated using the K–M non-parametric method (Lee and Helsel 2007). The average, minimum, and maximum compositions of iron oxides for each deposit type are listed in Table 3. Magnetite and hematite grains were averaged together as their chemical compositions in individual deposits do not show significant differences, as discussed below. For some deposits, additional details on the chemical composition of individual grains or analyses are used to illustrate some important features of the mineral chemistry of iron oxides.

Spider diagrams

Spider diagrams provide an overview of the compositional characteristics for iron oxides of a deposit type. Figure 2 illustrates average compositions of the 12 selected elements for each mineral deposit type. The average composition of each mineral deposit type is computed from the mean composition of all analyses of magnetite and hematite for each deposit in order to avoid overrepresentation of deposits with more analyses. The spider diagram is laid out from highest (Si) to lowest (K) average elemental abundance for the 12 elements selected, in order to generate smooth patterns with a gentle negative slope. Normalization to a range of crustal, mantle, or our database iron oxide average values has shown no additional benefit to simple concentration plots.

The spider diagram illustrating average composition of mineral deposit types (Fig. 2) shows that Ni-Cu deposits are characterized by high Ni and Cr, whereas skarns and Opemiska-type Cu veins are relatively rich in Ca. Although a low-Ti magnetite is commonly considered characteristic of IOCG deposits, our data indicates that this is a feature shared also by skarns, clastic-dominated Pb-Zn, VMS, Opemiska-type Cu veins, and BIF, which have even lower average Ti concentrations than those of IOCG deposits. Kiruna-type apatite–magnetite and Cu porphyry deposits have higher Ti and V concentrations than those of IOCG deposits, a feature that is discussed in more detail below. Kiruna-type apatite–magnetite deposits also show relatively low concentrations of Mn and Al. Iron oxides from Fe-Ti, V and Cr deposits can be easily identified by their characteristic enrichments in Ti, V and Cr, respectively.

Discriminant diagrams

Over the last 30 years, petrogenetic discriminant diagrams have evolved from a few to a wide range of grids that are used either for several rock types or have specific application to a rock type or process. Mineral chemistry discriminant diagrams allow determination of petrogenetic characteristics of xenocrystic grains in kimberlitic intrusions, a method widely employed in exploration for diamonds (Fipke et al. 1995). We take the same approach

Table 3 Mean, minimum and maximum compositions of iron oxides (magnetite and hematite) for each deposit type (*nd* not detected)

Deposit Type		Zn wt.%	Cu wt.%	Ni wt.%	Mn wt.%	Cr wt.%	V wt.%	K wt.%	Ca wt.%	Ti wt.%	Al wt.%	Si wt.%	Mg wt.%
IOCG (n=11)	Mean	0.043	0.044	0.025	0.045	0.013	0.039	0.009	0.025	0.042	0.109	0.163	0.171
	Min	0.033	0.024	0.018	0.010	0.005	0.008	0.002	0.004	0.003	0.025	0.008	0.007
	Max	0.054	0.093	0.031	0.128	0.077	0.116	0.028	0.119	0.131	0.247	0.555	1.175
Kiruna-type (n=7)	Mean	0.047	0.034	0.048	0.037	0.012	0.238	0.005	0.014	0.154	0.053	0.047	0.057
	Min	0.040	0.023	0.020	0.014	0.008	0.062	0.002	0.011	0.009	0.018	0.010	0.005
	Max	0.065	0.064	0.116	0.101	0.018	0.479	0.010	0.022	0.431	0.100	0.119	0.191
BIF (n=4)	Mean	0.061	0.031	0.029	0.018	0.021	0.015	0.003	0.009	0.014	0.036	0.138	0.013
	Min	0.034	0.024	0.025	0.015	0.014	0.011	0.002	0.003	0.009	0.014	0.020	0.007
	Max	0.084	0.047	0.039	0.022	0.041	0.022	0.005	0.015	0.022	0.056	0.296	0.018
Porphyry (n=13)	Mean	0.057	0.038	0.027	0.072	0.018	0.160	0.012	0.021	0.142	0.211	0.122	0.055
	Min	0.041	0.028	0.022	0.022	0.006	0.012	0.004	0.004	0.017	0.115	0.014	0.012
	Max	0.109	0.067	0.051	0.295	0.092	0.619	0.048	0.089	0.358	0.431	0.343	0.179
Skarn (n=15)	Mean	0.064	0.058	0.028	0.149	0.030	0.060	0.008	0.061	0.035	0.180	0.200	0.431
	Min	0.042	0.034	0.021	0.010	0.004	0.008	0.003	0.004	0.003	0.025	0.009	0.005
	Max	0.112	0.335	0.069	0.445	0.367	0.708	0.033	0.308	0.171	0.692	0.638	2.623
Fe-Ti (n=5)	Mean	0.050	0.037	0.027	0.138	0.172	0.498	0.002	0.009	6.240	0.503	0.028	0.317
	Min	0.043	0.026	0.023	0.018	0.010	0.052	0.002	0.002	0.797	0.026	0.014	0.011
	Max	0.059	0.050	0.041	0.353	0.527	0.958	0.003	0.015	10.170	1.861	0.048	0.879
V (n=1)		0.058	0.042	0.038	0.013	0.069	0.968	0.003	0.008	0.156	0.039	0.018	0.007
Cr (n=1)		0.085	0.027	nd	0.016	2.608	0.017	0.003	nd	nd	0.012	0.021	0.047
Ni-Cu (n=15)	Mean	0.086	0.039	0.113	0.132	0.325	0.142	0.003	0.017	0.345	0.133	0.061	0.047
	Min	0.045	0.026	0.033	0.017	0.008	0.007	0.002	0.003	0.008	0.009	0.016	0.006
	Max	0.282	0.079	0.318	0.384	1.711	0.408	0.010	0.135	1.851	0.610	0.226	0.142
VMS (n=17)	Mean	0.073	0.045	0.030	0.037	0.019	0.110	0.002	0.012	0.019	0.047	0.115	0.049
	Min	0.046	0.022	0.024	0.009	0.005	0.007	0.002	0.003	0.004	0.010	0.008	0.004
	Max	0.196	0.091	0.057	0.161	0.224	1.372	0.005	0.055	0.145	0.265	0.688	0.232
Clastic Pb-Zn	Mean	0.067	0.053	0.037	0.109	0.008	0.045	nd	0.006	0.039	0.061	0.015	0.019
(n=2)	Min	0.059	0.053	0.034	0.066	0.008	0.011	nd	0.006	0.039	0.026	0.014	0.012
	Max	0.075	0.053	0.039	0.151	0.008	0.080	nd	0.006	0.039	0.097	0.016	0.026
Archean porphyry	Mean	0.049	0.038	0.034	0.023	0.005	0.019	0.032	0.016	0.007	0.056	0.161	0.023
(n=4)	Min	0.039	0.026	0.022	0.008	0.007	0.008	0.004	0.006	0.003	0.018	0.012	0.006
	Max	0.064	0.040	0.057	0.066	0.026	0.030	0.102	0.045	0.012	0.170	0.458	0.054
Opemiska Cu veins	Mean	0.055	0.036	0.040	0.009	0.007	0.022	0.016	0.084	0.016	0.129	0.497	0.026
(n=8)	Min	0.048	0.025	0.024	0.007	0.005	0.010	0.002	0.005	0.004	0.014	0.103	0.005
	Max	0.076	0.077	0.081	0.018	0.011	0.033	0.039	0.208	0.025	0.285	0.851	0.113

here, which is to identify elements, element ratios, and/or element combinations that empirically plot one or several mineral deposit types in distinct fields in a binary diagram. Some diagrams uniquely discriminate samples from one mineral deposit type from all other types of deposits, whereas others allow several fields to be distinguished that are each characteristic for one mineral deposit type. Below, four discriminant diagrams are described in a sequence that allows most efficient identification of a mineral deposit type.

The Ni+Cr vs. Si+Mg diagram (Fig. 3) is efficient in separating the average magnetite composition of Ni-Cu deposits from the average composition of magnetite and/or hematite from all other deposit types. A Cr-magnetite from a podiform chromite deposit plots at high Ni+Cr values, above the field for Ni-Cu-PGE deposits. The field for Ni-Cu deposits is tentatively limited at low Si+Mg by the composition of magnetite from the GP4F sample, which is from a VMS deposit in the Finlayson Lake district (Yukon, Canada) that was affected by amphibolite-grade metamorphism (Layton-Matthews et al. 2008). The magnetite studied from the GP4F deposit is fractured, suggesting it may predate deformation, and occurs in a matrix of chlorite and hornblende within the sulfide lenses. It is uncertain if the magnetite studied belongs to the metamorphosed host

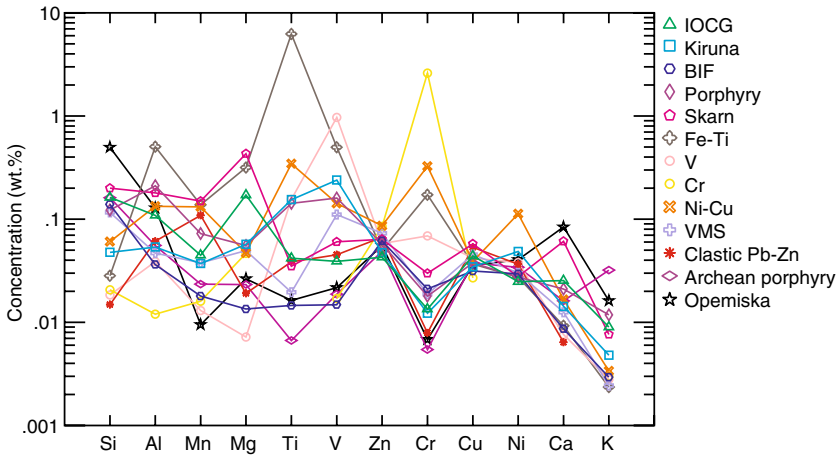

Fig. 2 Spider diagram showing the average composition of Fe-oxide minerals in various ore deposit types calculated using the Kaplan–Meier method for the 12 elements measured

rock or to the metamorphosed massive sulfides. In contrast, magnetite with pyrite inclusions from the nearby, and geologically similar, Kudz Ze Kayah VMS deposit (Layton-Matthews et al. 2008) plots below the field for Ni-Cu deposits in Fig. 3.

The Al/(Zn+Ca) vs. Cu/(Si+Ca) diagram (Fig. 4) effectively separates VMS deposits from all other deposit types with the exception of Ni-Cu deposits already identified using the Ni+Cr vs. Si+Mg diagram (Fig. 3). Magnetite in VMS deposits typically has high Si, Zn, and Ca, and low Al (Fig. 2). The field for VMS deposits is large, but excludes iron oxides from other deposit types with the exception of samples from the Faro Vangorda clastic-dominated Pb-Zn deposit (Yukon, Canada). Analysis of magnetite or hematite from more VMS deposits, subdivided by lithostratigraphic setting (Franklin et al. 2005), will likely provide more precise fields and/or discriminant diagrams for VMS and clastic-dominated Pb-Zn deposits, a subject of current research.

As shown previously, Ti and V concentrations in Fe-oxide minerals display strong variations related to deposit type (Fig. 2, Table 3). The sum of Ti+V is therefore useful to discriminate between mineral deposit types, in combination with either Ni/(Cr+Mn; Fig. 5) or Ca+Al+Mn (Fig. 6). Ni-Cu and VMS deposits, which can be identified using the Ni+Cr vs. Si+Mg diagram (Fig. 3) and the Al/(Zn+Ca) vs. Cu/(Si+Ca) diagram (Fig. 4), respectively, are not plotted in the Ni/(Cr+Mn) vs. Ti+V and Ca+Al+Mn vs. Ti+V diagrams because the latter two plots do not discriminate these deposit types.

In the Ni/(Cr+Mn) vs. Ti+V diagram (Fig. 5), fields for IOCG, Kiruna-type, porphyry Cu and Fe-Ti and V deposits are well defined. Fe-oxide minerals from skarns generally have low Ti+V concentrations, but display variable Ni/(Cr+Mn) ratios, preventing definition of a compositional field for skarn deposits in the Ni/(Cr+Mn) vs. Ti+V diagram. Fe-oxide compositions from BIF deposits plot in a cluster at low Ti+V and intermediate Ni/(Cr+Mn) but overlap with those from some skarn deposits (Fig. 5). Similarly, magnetites from Opemiska-type Cu veins have characteristic low Ti+V concentrations and high Ni/(Cr+Mn) ratios that overlap with those from Archean porphyry deposits, which also have low Ti+V concentrations, but display variable Ni/(Cr+Mn)

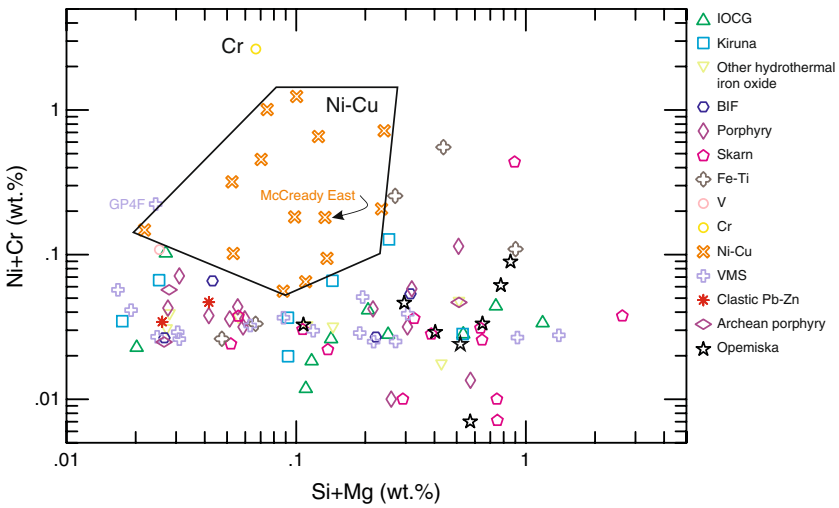

Fig. 3 Ni+Cr vs. Si+Mg discriminant diagram of average Fe-oxide deposit composition for Ni-Cu deposits compared to other deposit types

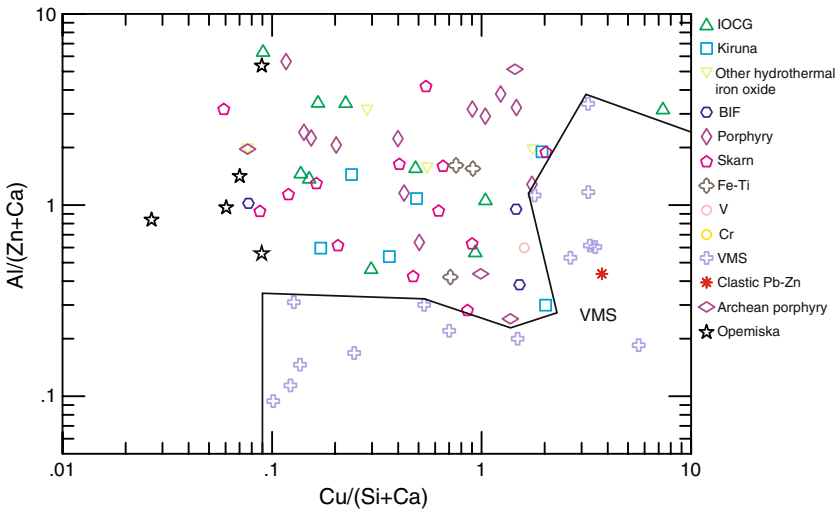

Fig. 4 Al/(Zn+Ca) vs. Cu/(Si+Ca) discriminant diagram for magnetite from VMS deposits

ratios. The low Ti+V of Archean porphyry deposits contrasts with the higher Ti+V values for Phanerozoic porphyry Cu deposits. No deposits listed as "Other hydrothermal iron oxide" (Table 2) plots in the field for IOCG deposits, but the Fort Constantine, Amargosa and San Fernando deposits plot in the field for Kiruna deposits (Fig. 5). The Osborne deposit is considered an IOCG deposit (Fisher and Kendrick 2008) but the copper–gold mineralization is known to overprint earlier magnetite BIF mineralization (Davidson and Large 1994, Williams 1994). Interestingly, magnetite from the Cu-Au mineralization from the Osborne mine plots in the field for BIF in the Ni/(Cr+Mn) vs. Ti+V diagram (Fig. 5). Carew (2004) similarly showed that the Osborne magnetite had a chemical composition different from that of the Ernest Henry IOCG deposit. The Queylus deposit plots close to the Osborne deposit (Fig. 5) but this deposit has a controversial mineral affinity as it is interpreted as an IOCG type by Furic and Jébrak (2005) but has been previously regarded as Archean porphyry type by Cimon (1973). Another hydrothermal iron oxide deposit, Murdie Island, plots near the junction of the fields for porphyry and IOCG deposits, while the Marcona deposit plots close to the field for skarn deposits (Fig. 5).

The Ca+Al+Mn vs. Ti+V diagram (Fig. 6) is useful to distinghuish skarn, IOCG, Kiruna-type, porphyry Cu, and Fe-Ti-V deposits. In this diagram, Fe-oxide minerals from BIF deposits plot in a cluster at low values of Ti+V and Ca+Al+Mn, a characteristic also shared by some Opemiska-type Cu vein and Archean porphyry deposits. A combination of both the Ni/(Cr+Mn) vs. Ti+V (Fig. 5) and Ca+Al+Mn vs. Ti+V (Fig. 6) diagrams is thus necessary to distinguish Fe-oxide minerals in BIF deposits from those in skarn, Opemiska-type Cu vein, and Archean porphyry deposits. Magnetites from Opemiska-type Cu veins plot close to both skarn and BIF deposit fields, but they can be distinguished from these two deposit types with the Ni/(Cr+Mn) vs. Ti+V diagram (Fig. 5). Magnetites from some Archean porphyry deposits plot close to magnetite from Opemiska-type Cu

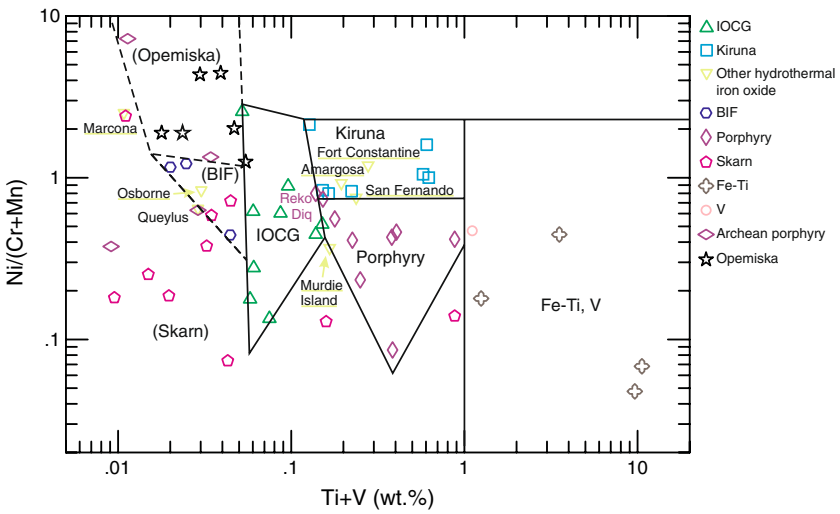

Fig. 5 Ni/(Cr+Mn) vs. Ti+V discriminant diagram for average Fe-oxide compositions from Kiruna, IOCG, porphyry Cu, Fe-Ti-V, and BIF deposits

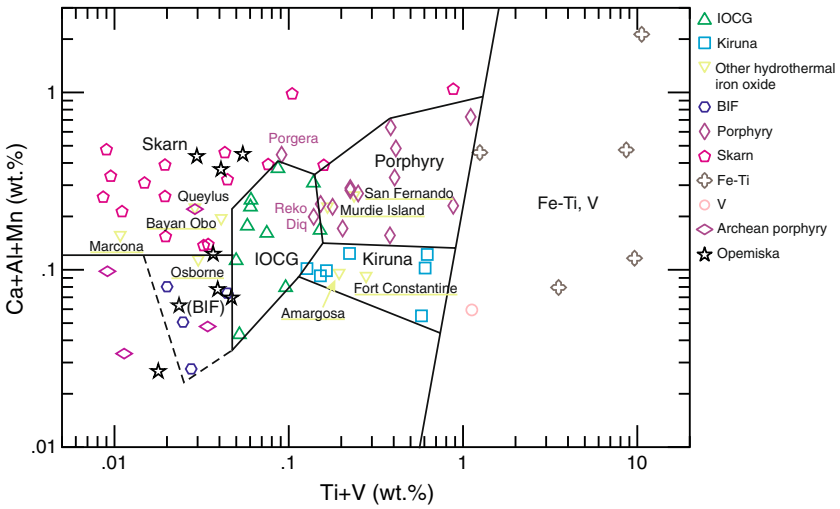

Fig. 6 Ca+Al+Mn vs. Ti+V discriminant diagram for average Fe-oxide compositions from Kiruna, IOCG, porphyry Cu, skarn, Fe-Ti-V, and BIF deposits

vein deposits, but the two deposit types cannot be isolated in specific fields. Data from the Porgera deposit plots slightly to the left of the field for porphyry deposits due to unusually low V content in that sample (Fig. 6). At Porgera, the magnetite-bearing veins are typical of deeper, pre-stage I magnetite-sulfide-quartz-carbonate veins, that are considered to belong to a stage of Cu porphyry style of mineralization in contrast to the more economically important stage II quartz-roscoelite-pyrite-gold epithermal gold mineralization (Ronacher et al. 2004). The unusual low V content of magnetite at Porgera is perhaps related to partitioning of V in abundant later-stage roscolite in this deposit. Fe-oxide minerals from "Other hydrothermal iron oxide" deposits essentially plot in the same fields as on the Ni/(Cr+Mn) vs. Ti+V diagram (Fig. 5), except for the San Fernando deposit, which plots in the field for Cu porphyry deposits rather than the field for Kiruna-type deposits, as in Fig. 6. Fe-oxide minerals from the Bayan Obo Fe-REE-Nb deposit have Ni contents too low to plot on the Ni/(Cr+Mn) vs. Ti+V diagram (Fig. 5), and plot in the field for skarns, very close to the field for IOCG deposits in Fig. 6. The Bayan Obo deposit consists of multistage mineralisation that has been attributed to a subgroup of iron oxides deposits (Groves et al. 2010) and to the class of carbonatite deposits (Smith 2007),

Flow chart for discriminant diagrams

We have shown that there are systematic variations in the composition of magnetite and hematite that are related to specific types of mineral deposits, and we have devised a series of diagrams that are useful to ascribe magnetite and hematite to these deposit types. Some of these discriminant diagrams are useful to separate one deposit type from all other types, whereas other diagrams allow distinction of several mineral deposit types. Figure 7 presents an interpretation flow sheet that facilitates identification of the deposit types investigated in this study. First, the average composition of magnetite and hematite can be attributed to Ni-Cu deposits using the Ni+Cr vs. Si+Mg discriminant diagram (Fig. 3). In a second step, magnetite and hematite plotting outside the field for Ni-Cu deposits in the Ni+Cr vs. Si+Mg diagram is screened for VMS and perhaps clastic-dominated Pb-Zn deposits using the Al/(Zn+Ca) vs. Cu/(Si+Ca) diagram (Fig. 4). The final, third step, utilizes the Ni/(Cr+Mn) vs. Ti+V (Fig. 5) and the Ca+Al+Mn vs. Ti+V (Fig. 6) diagrams to discriminate IOCG, Kiruna, BIF, porphyry Cu, skarn, and Fe-Ti-V deposits.

Comparison of magnetite and hematite composition

We use the Ca+Al+Mn vs. Ti+V diagram to determine if there are significant chemical differences between the average magnetite and hematite composition either in samples, or in deposits, where both coexist. The samples studied from Ni-Cu-PGE, VMS, clastic-dominated Pb-Zn, Opemiska-type Cu vein, Archean porphyry or Fe-Ti-V deposit samples did not contain hematite. For most IOCG, Kiruna, and porphyry Cu deposits, we find replacement of magnetite by hematite (martite), and less common replacement of hematite by magnetite (mushketovite). In these deposits, we observe slight differences in average composition, both for Ti+V and Ca+Al+Mn contents (Fig. 8). These differences arise from average sample composition rather than significant compositional variations between magnetite and hematite in one sample. For skarn and BIF deposits, the proportion of deposits containing both magnetite and hematite is much lower, with greater variations between iron oxide compositions, but which is also related to different samples. The Jaima skarn deposit (Tibet, China; Beaudoin et al. 2005) shows compositional difference between magnetite and hematite, where acicular hematite, associated with chalcopyrite or garnet in the

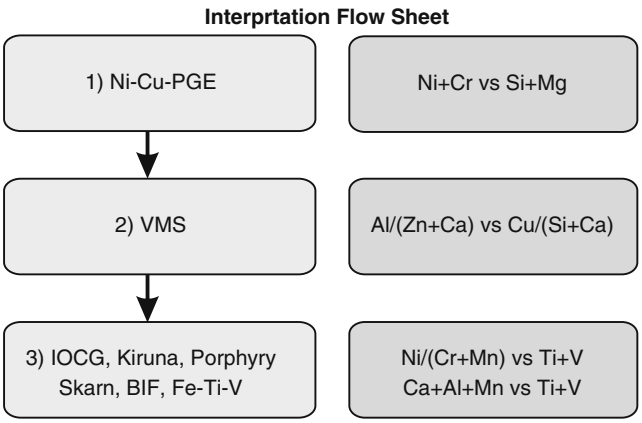

Fig. 7 Flowchart for discriminating deposit types based on iron oxide mineral compositions

calcite–wollastonite matrix, plots in the field for skarn deposits (Fig. 8). Magnetite from Jaima is closely associated with galena and contains chalcopyrite inclusions, which suggests it formed after chalcopyrite and hematite in a later paragenetic stage. The Jaima magnetite has low abundances of all the elements used in the Ca+Al+Mn vs Ti+V diagram (Fig. 8). This is the only Cu-Pb-Zn skarn deposit that we have investigated, and the geological context of this deposit is not known in sufficient details to explain the compositional difference between magnetite and hematite.

The El Laco Kiruna-type and PUT2 skarn deposits are used as examples to illustrate compositional variations between magnetite and hematite (Fig. 9). The average composition of magnetite and hematite are similar from El Laco and PUT2 deposits, and the El Laco and PUT2 deposit samples display larger compositional variation between samples than for individual analyses within a

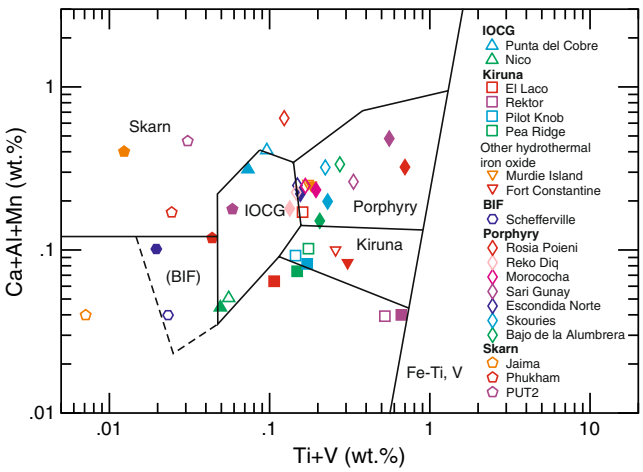

Fig. 8 The Ca+Al+Mn vs. Ti+V discriminant diagram for average compositions of magnetite (*empty symbol*) and hematite (*filled symbol*) in various deposit types. Each *color* represents the average composition for magnetite and hematite in one deposit

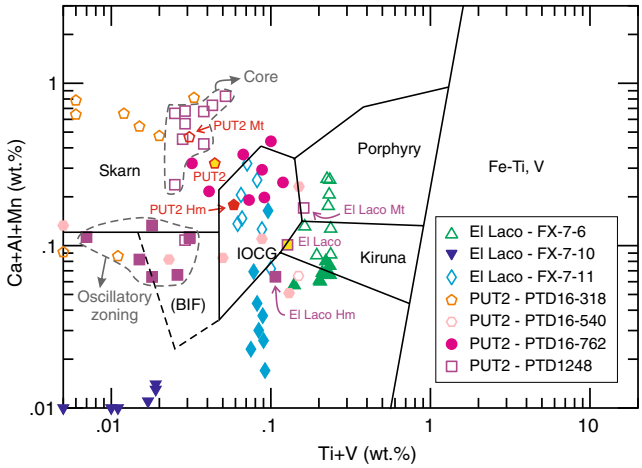

Fig. 9 The Ca+Al+Mn vs. Ti+V discriminant diagram showing individual spot analyses of magnetite (*empty symbol*) and hematite (*filled symbol*) from the El Laco Kiruna-type and PUT2 skarn deposits. Averages for magnetite and hematite in one deposit, and for all analyses in each deposit are highlighted

sample (Fig. 9). The El Laco deposit is characterized by martite replacement. Magnetite and hematite grains from El Laco have limited range in Ti+V for each sample (Fig. 9). In sample FX-7-10, martite replacement is complete and hematite has lowest El Laco Ti+V (Fig. 9). Typically, magnetite has higher Ca+Al+Mn than hematite, mostly as result of high Ca content in magnetite, as shown for both individual analyses and deposit magnetite and hematite averages (Fig.9). PUT2 deposit samples display larger compositional variation between samples (Fig. 9). For example, PTD16-318 sample contains only magnetite poor

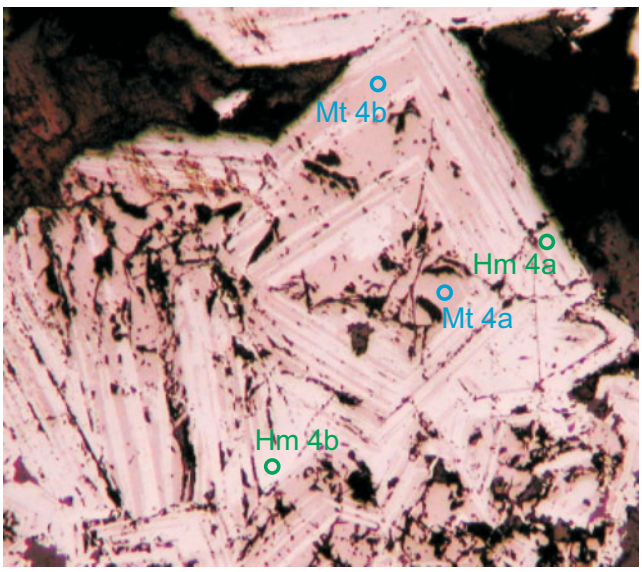

Fig. 10 Microphotograph of sample PTD1248 from PUT2 skarn deposit showing magnetite cores surrounded and partly replaced by magnetite and hematite oscillatory zoning. Analysis spots for magnetite and hematite are shown with labels

in V, whereas sample PTD16-762 contains only hematite with higher V (Fig. 9). Sample PTD16-540 contains disseminated martite grains that are small and fractured. They show highly variable Ti+V concentrations and generally low Ca+Al+Mn (Fig. 9). Sample PTD1248 contains grains with a core of fractured magnetite surrounded and partly replaced by oscillatory magnetite and hematite zoning (Fig. 10). Core magnetite analyses ("Mt 4a", Fig. 10) have high Ca and Al concentrations typical of skarn, whereas magnetite and hematite analyses from the second stage oscillatory zoning ("Mt 4b", "Hm 4a" and "Hm 4b", Fig. 10) have lower concentrations of these elements (Fig. 9).

In summary, the average composition of magnetite or hematite in one deposit plots near the average for all analyses for a deposit. This is an unexpected observation considering that reduction of hematite to magnetite, or mushketovite, involves reductive dissolution of hematite to $Fe_{(aq)}^{2+}$ followed by non-redox transformation of hematite and $Fe_{(aq)}^{2+}$ to magnetite in low temperature hydrothermal systems (Otake et al. 2010). The compositional variability is mostly between different samples rather than due to systematic differences between magnetite and hematite composition. Analyzing several grains of magnetite and martite, or hematite and mushketovite, yields a representative average composition for a deposit, such that analysis of martite or mushketovite should be included in the calculation of average composition of a mineral deposit to avoid arbitrary selection of iron oxide grains.

Chemical composition variance in deposit

The Reko Diq porphyry Cu deposit has the most samples (seven) and total analyses with 41 magnetite and 60 hematite grains analyzed (Table 2). Reko Diq's individual analyses are plotted in the Ca+Al+Mn vs. Ti+V discriminant diagram to illustrate variance in composition within a deposit (Fig. 11). As shown for the El Laco and PUT2 deposits, the Reko Diq samples show that chemical composition variation within a deposit is mostly related to difference in composition between samples, rather than variation of composition within one sample. Considering Reko Diq, the average composition of four of the seven samples plot in the field for porphyry Cu deposits (Fig. 11). Of the three sample averages that plot outside the field for porphyry Cu deposits, one (H13-Loc 18) plots at Ti+V slightly lower than the boundary for porphyry Cu deposits, whereas samples H14-Loc 25 and H15-TAF averages have low Ti+V and plot in the field for Kiruna-type deposits. These variations in Ti+V values in Reko Diq samples are a consequence of rutile exsolution in hematite, as discussed below.

Effects of oxidation–exsolution on average composition

In high temperature magmatic systems that formed Fe-Ti and Ni-Cu deposits, and some high temperature hydrothermal deposits such as porphyry Cu and Kiruna-type deposits, sub-solidus exsolution and/or oxidation processes can modify the chemical composition of magnetite. Al, Mg, and Cr are enriched in the spinel exsolution lamellae, whereas the host mineral is depleted in these elements. Figure 12 shows the composition of analyses from Sudbury deposits in the Ni+Cr vs. Si+Mg diagram. The range of magnetite individual analyses straddles the boundary of the field defined by the average composition of Ni-Cu deposits (Fig. 3) whereas the average composition for most samples plot in the field for Ni-Cu deposits (Fig. 12). The average composition of magnetite from a few samples from the Levack and McCready East deposits plot outside, but close to, the field for Ni-Cu deposits (Fig. 12). As an example, magnetite spot analyses from sample RX168 (McCready East deposit) range between low and high Si+Mg values about the mean for this sample (Fig. 12). SEM-backscattered images of sample RX168 illustrate that grains with microscopic spinel exsolution that cannot be avoided during analysis (Fig. 13a) yield high Mg values in magnetite therefore plotting at high

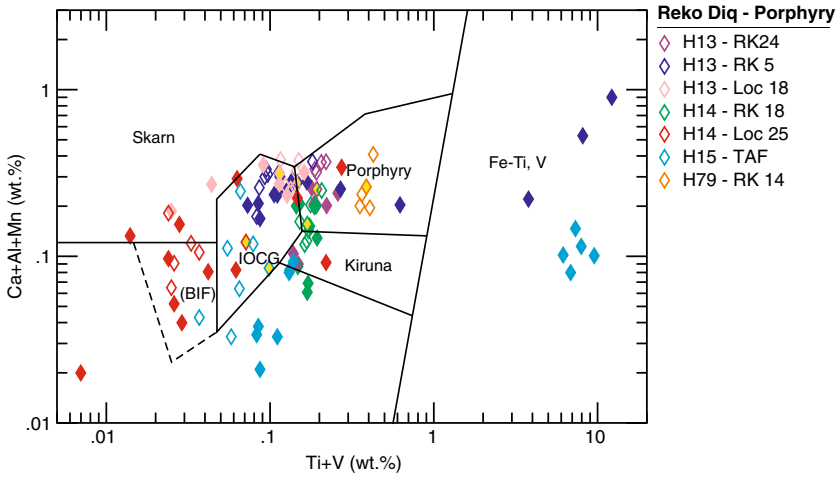

Fig. 11 The Ca+Al+Mn vs. Ti+V discriminant diagram showing individual analyses of magnetite (*empty symbol*) and hematite (*filled symbol*) for samples from the Reko Diq porphyry Cu deposit. Average for each sample is the *symbol filled with yellow*

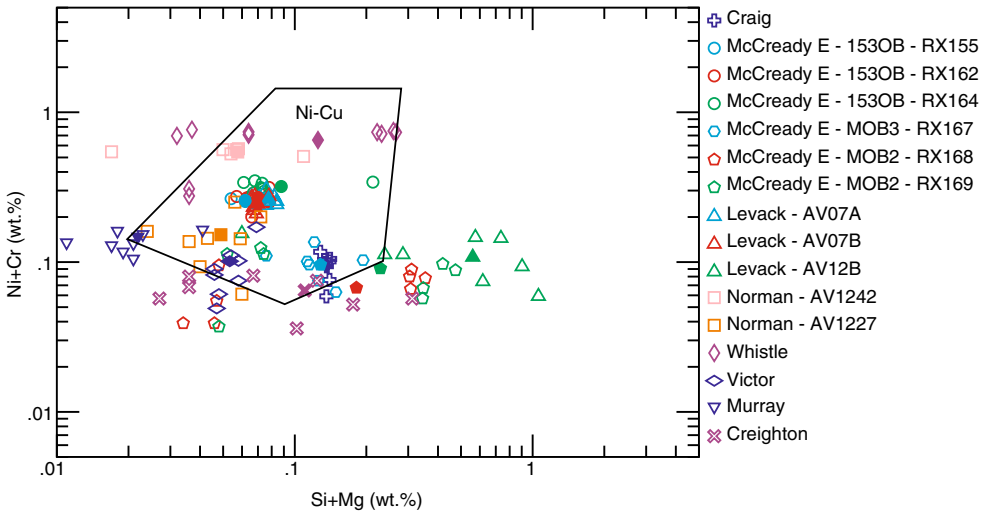

Fig. 12 The Ni+Cr vs. Si+Mg discriminant diagram showing individual magnetite analyses from Sudbury Ni-Cu deposits. Sample average is shown as *filled symbol*

Si+Mg values in Fig. 12, whereas analyses for magnetite grains in which exsolved spinel has migrated into larger inclusions, leaving grain sectors with sub-micrometer spinel exsolutions (Fig. 13b), are depleted in Mg, and therefore plot at low Si+Mg values in Fig. 12.

Similarly, the variations in Ti+V values in Reko Diq samples (Fig. 11) are explained by the presence of rutile lamellae in hematite, which varies in scale and abundance from one sample to another. As an example, magnetite and hematite spot analyses from sample H13-RK 5 have Ti+V values ranging from less than 0.08 wt.% to more than 12 wt. % (Fig. 11). Hematite grains with small rutile lamellae that cannot be avoided during analysis yield high Ti values in hematite therefore plotting at high Ti+V values in Fig. 11. Magnetite and martite grains free of rutile lamellae are depleted in Ti, and plot at low Ti+V values in Fig. 11.

For grains affected by oxidation–exsolution, our data suggest that analysis of several areas of grains with various proportions of inclusions can yield an average composition similar to that of the grain prior to oxidation–exsolution. Analyzing several grains with varying proportions of oxidation-exsolution inclusions yields an average composition interpreted to be representative of the deposit iron oxide composition. A similar observation is made for ilmenite oxidation–exsolution inclusions, which is typical of Fe-Ti deposits characterized by Ti enrichment in magnetite.

Discussion

Representativeness of the dataset

In this study, some deposits (for example, Windy Craggy or Reko Diq) or types of deposits (for example Ni-Cu massive sulfides) have been studied in more detail than other deposits or deposit types (Table 2). Despite the uneven detail of investigation, the selected examples of Ni-Cu massive sulfides, porphyry Cu, VMS, and IOCG deposits display a range of deposits considered typical for these deposit type (Table 2). For these deposit types studied in more detail, the selected deposits represent a range of geologic settings, display a range of age of formation, and cover some of the important subdivisions of these major mineral deposit classes. As an example, the IOCG deposits investigated comprise the most prominent examples of this class such as Olympic Dam, Ernest Henry, and Candelaria, which range in age from Proterozoic to Mesozoic. The VMS deposits studied comprise examples formed in four of the five lithotectonic settings recognized for this deposit type (Franklin et al. 2005), range in age from Archean (ex. Ansil) to Recent (ex. ODP Mound), and have been affected by sub-greenschist to amphibolite metamorphism. The Ni-Cu massive sulfide examples represent various geologic settings from the Sudbury district, to dykes in anorthosite complexes (Voisey's Bay), to subvolcanic intusions (ex. Katiniq, Pipe). Other deposit types are less well represented with only a few deposits studied, for example, four BIF and two clastic-dominated Pb-Zn deposits have been investigated so far, such that our knowledge of the composition of iron oxides in these less well-documented deposit types remains preliminary. On the other hand, even if Cr, Fe-Ti, and V deposits are represented by fewer analyses (Table 2), their chemical composition is characteristic enough to allow their classification within the discriminant diagrams presented in this paper. Finally, some deposit types have not been studied, such as diamond-bearing kimberlite and lamproite, and various types of gold deposits.

Partitioning of trace and minor elements in iron oxides

Iron and titanium minerals have been widely used as a thermo-oxybarometer based on $Fe^{2+}+Ti^{4+}$ for 2 Fe^{3+}

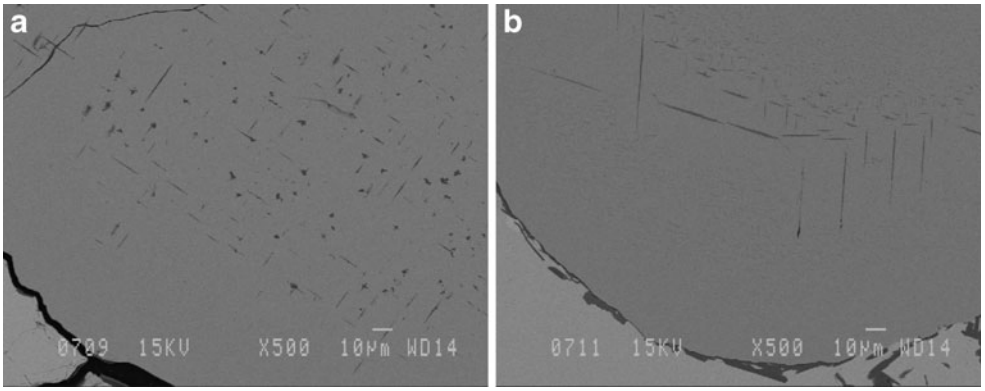

Fig. 13 SEM backscattered electron images of sample RX168 from the McCready East Sudbury Ni-Cu deposit. **a** Magnetite with large spinel exsolution (*dark gray*), and **b** margin of a magnetite grain without large spinel inclusions (*dark gray*)

exchange and iron redox equilibrium between magnetite, hematite, ulvospinel, and ilmenite (Buddington and Lindsley 1964; Sack and Ghiorso 1991; Sauerzapf et al. 2008). Despite extensive experimental evidence and theoretical modeling, significant uncertainty remains on the calibration of the thermo-oxybarometer at temperature below 600°C and for oxides with minor concentration (<6 wt.%) of Al_2O_3, MgO, MnO, and Cr_2O_3 (Sauerzapf et al. 2008). Partitioning of Ni, Ca, Co, and Mn between mafic melt and magnetite is independent of oxygen fugacity (Toplis and Corgne 2002). These divalent cations have small (Mn ~1–4) to moderate (Ni ~20–100) magnetite-liquid partition coefficients (Toplis and Corgne 2002). Vanadium partitioning, in contrast, is decreasing with higher oxygen fugacity, and has a higher mineral-liquid partition coefficient in magnetite (~ 0.4–1.5) than clinopyroxene (Toplis and Corgne 2002). Partitioning of Ni and Co in spinel is less dependent on temperature or oxygen fugacity than on the spinel composition (Righter et al. 2006). In the Kerimasi (Tanzania) carbonatite, magnetite becomes depleted in Mg with magma evolution whereas Mn is shown to be more compatible with increasing oxygen fugacity, in contrast to vanadium (Reguir et al. 2008). Magnetites from carbonatite typically contain trace amounts of Zn, Cr, Ni,Co, Zr, Hf, Nb, Ta, Ga (Reguir et al. 2008). Partition of Zr, Nb, Ta, and Hf between magnetite and mafic to intermediate silicate melts is strongly controlled by the Ti and Al content of magnetite (Nielsen and Beard 2000). HFS elements are more incompatible relative to Ti in magnetite at lower temperature and/or lower pressure (Nielsen and Beard 2000). Magmatic partitioning of trace elements in magnetite is a complex function of melt composition, temperature, pressure, oxygen fugacity, and major element composition of the magnetite. Magnetite crystallized from evolving silicate, carbonatitic or sulfide melts will incorporate a range of trace elements, from divalent metals such as Ni, to HFS elements. The average concentrations of several elements (e.g., Ni), typical for magmatic deposit types, are however significantly higher from those of other types of mineral deposits (Fig. 2).

Knowledge of trace element partitioning between iron oxides and hydrothermal solutions is even less well understood. Synthetic magnetite, doped in minor to trace amounts of Cr, Mn, Co, Ni, Cu, La, Nd, and Gd, is commonly precipitated from low temperature (<300°C) solutions to produce magnetite nanoparticles (Diamandescu et al. 1998; Wang et al. 2009). At high temperature (600–800°C), Mn, Zn, Cu, and Cd are strongly partitioned in the chloride solution relative to Fe, and the divalent metals partitioning in the chloride solution increases with lower temperature (Ilton and Eugster 1989). Taking Mn as an example, our data show no systematic trend in average Mn content of iron oxides and the temperature of formation of the mineral deposit types investigated. For example, the highest average Mn is measured not only in high temperature magmatic Ni-Cu, Fe-Ti, and hydrothermal skarn deposit-types but also in low-temperature clastic-dominated Pb-Zn deposits (Fig. 2). Porphyry-Cu, IOCG and Kiruna-type high-temperature hydrothermal deposits have intermediate average Mn similar to lower temperature VMS deposits. If low temperature BIFs have low average Mn, this is also found in magmatic Cr and V deposits (Fig. 2), thus showing that several physico-chemical parameters other than temperature, such as hydrothermal solution composition, pH, and oxygen fugacity, are important parameters that control partitioning of trace elements in hydrothermal iron oxides.

Comparison with other studies of iron oxides

LA-ICP-MS analyses have lower detection limits, and a wider range of minor and trace elements can thus be analyzed and used in studies of the chemical composition of iron oxides from ore deposits and their hostrocks (e.g., Carew 2004; Singoyi et al. 2006; Rusk et al. 2009; Nadoll et al. 2009). It is noteworthy that eight elements out of ten that have concentrations commonly above the detection limit using the LA-ICP-MS (Mg, Al, Ti, V, Mn, Ni, Zn, and Sn; Singoyi et al. 2006; Rusk et al. 2009) also yield accurate and precise results using the electron microprobe method used in this study (Table 1). Only two elements (Co and Ga) have concentrations that are too low for analysis by

EMPA. Moreover, 11 out of the 14 elements (Ti, Si, Al, Mg, V, Cr, Mn, Ni, Cu, Zn, Sn) detected in magnetite using the LA-ICP-MS method by Carew (2004) are also measured using EMPA method, whereas only three elements measured by Carew (2004) are not detected by EMPA. EMPA spot analyses have a higher spatial resolution (<10 μm) compared to lower spatial resolution for LA-ICP-MS analyses (>50 μm) such that EMPA analyses are less susceptible to contamination by small inclusions in the mineral of interest. In addition, the EMPA allows selecting analytical spot to avoid submicrometric inclusions using a combination of polarized light and backscattered electron images.

According to Carew (2004), trace element patterns for Kiruna-type deposits from Sweden and Chile are different from those of the Cloncurry district IOCG mineralization, as also shown here in Figs. 2, 5, and 6. In addition, Carew (2004) showed that magnetite from U-Au mineralization at the Osborne deposit has a different trace element composition compared to that of the Ernest Henry IOCG deposit, a conclusion also reached by our study, where samples of breccia cemented by pyrite and magnetite from the Osborne deposit have an average composition that plots in the field for BIF deposits (Figs. 5 and 6). Based on the trace element composition of magnetite from selected VMS, skarn, IOCG, and Broken Hill-type clastic-dominated Pb-Zn deposits from Australia, Singoyi et al. (2006) concluded that magnetite incorporates trace elements that are typical for a specific deposit type. In particular, they showed that the Sn/Ga vs. Al/Co diagram has potential to distinguish the deposit types that they studied. We cannot plot our data in the Sn/Ga vs. Al/Co discriminant diagram because Ga and Co are not measured with the EMPA. However, we propose other discriminant criteria to similarly discriminate between VMS, skarn and IOCG types of deposits (Figs. 4, 5, 6). Finally, Rusk et al. (2009) and Nadoll et al. (2009) reported differences in chemistry between magnetite from ore deposits and their related hostrocks. They concluded that the difference in magnetite chemistry likely results from mineral equilibrium assemblage at the site of magnetite deposition (Rusk et al. 2009), and that these chemical differences may be a useful pathfinder for orebodies in various geologic settings (Nadoll et al. 2009). The iron oxide compositional data we present in this paper is entirely derived from mineralized rocks, such that it cannot be compared to the composition of iron oxides from rocks barren of mineralization, which is a subject of ongoing research.

Conclusions

The electron microprobe is a widely available instrument that allows fast, efficient, and low-cost analysis of iron oxides for application to mineral exploration. The chemical composition of iron oxides magnetite and hematite can be used to fingerprint mineral deposit types as shown by several studies (Carew 2004; Gosselin et al. 2006; Singoyi et al. 2006; Beaudoin et al. 2007; Rusk et al. 2009; Nadoll et al. 2009). The discriminant diagrams presented in this paper can be used to identify a mineral deposit type according to magnetite or hematite compositions, but the reference database is composed of magnetite and hematite sampled from mineralized rocks only. A set of discriminant diagrams has been devised that enables distinction of a wide range of mineral deposit types using a multi-step approach that is most efficient for fingerprinting a mineral deposit based on its iron oxide composition. Discriminant diagrams such as the Ni+Cr vs. Si+Mg diagram for Ni-Cu-PGE deposits, and the Al/(Zn+Ca) vs. Cu/(Si+Ca) diagram for VMS and clastic-dominated Pb-Zn deposits are useful to distinguish these types of deposits. Other diagrams such as the Ni/(Cr+Mn) vs. Ti+V or the Ca+Al+Mn vs. Ti+V are not discriminant for Ni-Cu-PGE and VMS deposits, but are useful to distinguish IOCG from Kiruna-type, porphyry Cu, BIF, skarn, and Fe-Ti-V deposits.

Acknowledgments This research has been funded by the DIVEX research network, the Geological Survey of Canada and the Natural Science and Engineering Research Council of Canada Discovery Grant to GB. We would like to thank our colleagues in industry, government, and academia that have donated the samples used for this study: Doug Kirwin (Ivanhoe Mines Ltd.), Mark Cruise (Cardero Resources Corp.), Tim Fletcher (Barrick Gold UK Limited), Danielle Giovenezzo (formely Xstrata Nickel), Bruce Durham (Canadian Royalties Inc.), Peter Lightfoot (Vale), Gilles Roy (Xstrata Zinc), Patrice Roy (Géologie Québec), Louise Corriveau, Isabelle McMartin, Dorren E. Ames, Beth McClenaghan and Jan Peter (GSC), Marc Constantin, Éric David, Marjorie Simard (Université Laval), Michel Gauthier, Michel Jébrak and Renan Furic (UQAM), Olivier Côté-Mantha (UQAC), Jeremy P. Richards (University of Alberta), Meghan Jackson, Paul Jago and Janina Micko (University of British Columbia), Larry Meinert (Smith College), Jochen Kolb (RWTH Aachen University), Luis Fontboté, Aldo Bendezu, and Kalin Kouzmanov (Université de Genève), Khin Zaw (University of Tasmania). Marc Choquette has provided outstanding technical support with the microprobe analyses. Editor Patrick Williams and two anonymous reviewers provided numerous comments that improved significantly the paper.

References

Ancey M, Bastenaire F, Tixier R (1978) Application des méthodes statistiques en microanalyse. In: Maurice F, Meney L, Tixier R (eds) Microanalyse, microscopie électronique à balayage. Les Éditions du Physicien, Orsay, pp 323–347

Barnes SJ, Roeder PL (2001) The range of spinel compositions in terrestrial mafic and ultramafic rocks. J Petrol 42:2279–2302

Beaudoin G, Hébert R, Wang CS, Tang J (2005) Epithermal Au-Ag-Cu, porphyry Cu-(Au-Mo) and Cu-Au-Ag-Zn-Pb skarn deposits of the Gangdese Arc, Tibet. In: Mao J, Bierlein FP (eds) Eighth biennial SGA meeting: mineral deposit research: meeting the global challenge. Springer, Beijing, pp 1219–1222

Beaudoin G, Dupuis C, Gosselin P, Jébrak M (2007) Mineral chemistry of iron oxides: application to mineral exploration. In: Andrew CJ (ed) Ninth Biennial SGA meeting. SGA, Dublin, pp 497–500

Belousova EA, Griffin WL, O'Reilly SY, Fisher NI (2002) Apatite as an indicator mineral for mineral exploration: trace–element compositions and their relationship to host rock type. J Geochem Explor 76:45–69

Buddington AF, Lindsley DH (1964) Iron–titanium oxide minerals and synthetic equivalents. J Petrol 5:310–357

Carew MJ (2004) Controls on Cu-Au mineralisation and Fe oxide metasomatism in the Eastern Fold Belt, N.W. Queensland, Australia. Unpublished Ph.D. thesis, James Cook University

Cimon J (1973) Possibility of an Archean porphyry copper in Quebec. Can Min J 94:97

Davidson GJ, Large RR (1994) Gold metallogeny and the copper–gold association of the Australian Proterozoic. Miner Deposita 29:208–223

Deer WA, Howie RA, Zussman J (1992) An introduction to rock-forming minerals, 2nd edn. Longman, Harlow, Wiley, New York

Diamandescu L, Mihaila-Tarabasanu D, Teodorescu V, Popescu-Pogrion N (1998) Hydrothermal synthesis and structural characterization of some substituted magnetites. Mater Lett 37:340–348

Fipke CE, Gurney JJ, Moore RO (1995) Diamond exploration techniques emphasising indicator mineral geochemistry and Canadian examples. GSC Bull 423

Fisher L, Kendrick M (2008) Metamorphic fluid origins in the Osborne Fe oxide-Cu-Au deposit, Australia: evidence from noble gases and halogens. Miner Deposita 43:483–497

Franklin JM, Gibson HL, Jonasson IR, Galley AG (2005) Volcanogenic massive sulfide deposits. Econ Geol 100th Anniversary Vol:523–560.

Fraser JF (1993) The Lac Troilus gold–copper deposit, Northwestern Quebec: a possible Archean porphyry system. Econ Geol 88:1685–1699

Furic R, Jébrak M (2005) Archean IOCG deposit in a fluidized dilational jog (Chibougamau, Abitibi, Canada). Geol Soc Amer Abstr Program 37:516

Gosselin P, Beaudoin G, Jébrak M (2006) Application of the geochemical signature of iron oxides to mineral exploration. GAC-MAC Annual Meeting Prog Abs 31:CD-ROM

Griffis AT (1979) An Archean "porphyry-type" disseminated copper deposit, Timmins, Ontario—a discussion. Econ Geol 74:695–696

Grigsby JD (1990) Detrital magnetite as a provenance indicator. J Sed Petrol 60:940–951

Groves DI, Bierlein FP, Meinert LD, Hitzman MW (2010) Iron oxide copper-gold (IOCG) deposits through earth history: implications for origin, lithospheric setting, and distinction from other epigenetic iron oxide deposits. Econ Geol 105:641–654

Hall JM, Fischer JF (1977) Opaque mineralogy of basement rocks, Leg 37. Init Rep Deep Sea Drill Proj 37:857–873

Heimann A, Spry PG, Teale GS (2005) Zincian spinel associated with metamorphosed Proterozoic base-metal sulfide occurrences, Colorado: a re-evaluation of gahnite composition as a guide in exploration. Can Miner 43:601–622

Helsel D (2005) Nondetects and data analysis. Wiley, New York

Hitzman MW, Oreskes NO, Einaudi MT (1992) Geological characteristics and tectonic setting of Proterozoic iron oxide (Cu-U-Au-REE) deposits. Precambrian Res 58:241–287

Hutton CO (1950) Studies of heavy detrital minerals. GSA Bull 61:635–713

Ilton ES, Eugster HP (1989) Base metal exchange between magnetite and a chloride-rich hydrothermal fluid. Geochim Cosmochim Acta 53:291–301

Jarosewich E, Nelen JA, Norberg JA (1980) Reference samples for electron microprobe analysis. Geostand Newsl 4:43–47

Johnson HP (1979) Opaque mineralogy of the igneous rock samples from DSDP hole 395A. Init Rep Deep Sea Drill Proj 45:407–420

Layton-Matthews D, Peter JM, Scott SD, Leybourne M (2008) Distribution, mineralogy, and geochemistry of selenium in felsic volcanic-hosted massive sulfide deposits of the Finlayson Lake district, Yukon Territory, Canada. Econ Geol 103:61–88

Leach DL, Bradley DC, Huston D, Pisarevsky SA, Taylor RD, Gardoll SJ (2010) Sediment-hosted lead–zinc deposits in Earth history. Econ Geol 105:593–625

Lee L, Helsel D (2007) Statistical analysis of water-quality data containing multiple detection limits II: S-language software for nonparametric distribution modelling and hypothesis testing. Comput Geosci 33:696–704

Morton A, Yaxley G (2007) Detrital apatite geochemistry and its application in provenance studies. In: Arribas J, Critelli S, Johnsson MJ (eds) Geol Soc Amer Spec Paper 420:319–344

Nadoll P, Mauk JL, Hayes, TS, Koenig AE, Hofstra AH, Box SE (2009) Geochemistry of magnetite from hydrothermal ore deposits and their host rocks in the Proterozoic Belt Supergroup, USA. In: Williams et al. (eds) Smart science for exploration and mining, Proc 10th Biennial Meeting, Townsville, pp 129–131

Nielsen RL, Beard JS (2000) Magnetite-melt HFSE partitioning. Chem Geol 164:21–34

Otake T, Wesolowski DJ, Anovitz LM, Allard LF, Ohmoto H (2010) Mechanisms of iron oxide transformations in hydrothermal systems. Geochim Cosmochim Acta 74:6141–6156

Pettijohn FJ, Potter PE, Siever R (1987) Sand and sandstone (2nd ed.), Springer, New York, pp 553

Pilote P, Guha J (1998) Métallogénie de l'extrémité est de la sous-province de l'Abitibi. In: Pilote (ed) Géologie et métallogénie du district minier de Chapais-Chibougamau; nouvelle vision du potentiel de découverte, DV 98-03, MNRF Québec, Canada, pp 29–44

Ramdohr P (1980) The ore minerals and their intergrowths. Pergamon, New York

Razjigaeva NG, Naumova VV (1992) Trace element composition of detrital magnetite from coastal sediments of Northwestern Japan Sea for provenance study. J Sed Petrol 62:802–809

Reguir EP, Chakhmouradian AR, Halden NM, Yang P, Zaitsev AN (2008) Early magmatic and reaction-induced trends in magnetite from the carbonatites of Kerimasi, Tanzania. Can Miner 46:879–900

Righter K, Leeman WP, Hervig RL (2006) Partitioning of Ni, Co and V between spinel-structured oxides and silicate melts: Importance of spinel composition. Chem Geol 227:1–25

Ronacher E, Richards JP, Reed MH, Bray CJ, Spooner ETC, Adams PD (2004) Characteristics and evolution of the hydrothermal fluid in the North zone high-grade area, Porgera gold deposit, Papua New Guinea. Econ Geol 99:843–867

Rusk B, Oliver N, Brown A, Lilly R, Jungmann D (2009) Barren magnetite breccias in the Cloncurry region, Australia; comparisons to IOCG deposits. In: Williams et al. (eds) Smart science for exploration and mining, Proc 10th Biennial Meeting, Townsville, pp 656–658

Sack RO, Ghiorso MS (1991) An internally consistent model for the thermodynamic properties of Fe−Mg-titanomagnetite-aluminate spinels. Contrib Mineral Petrol 106:474–505

Sauerzapf U, Lattard D, Burchard M, Engelmann R (2008) The titanomagnetite–ilmenite equilibrium: new experimental data and thermo-oxybarometric application to the crystallization of basic to intermediate rocks. J Petrol 49:1161–1185

Scheka SA, Platkov AV, Vezhosek AA, Levashov GB, Oktyabrsky RA (1980) The trace element paragenesis of magnetite. Nauka, Moscow, p 147

Sillitoe RH (2010) Porphyry copper systems. Econ Geol 105:3–41

Singoyi B, Danyushevsky L, Davidson GJ, Large R, Zaw K (2006) Determination of trace elements in magnetites from hydrothermal

deposits using the LA ICP-MS technique. SEG Keystone Conference, Denver, USA: CD-ROM

Smith MP (2007) Metasomatic silicate chemistry at the Bayan Obo Fe-REE-Nb deposit, Innner Mongolia, China: contrasting chemistry and evolution of fenitising and mineralising fluids. Lithos 93:126–148

Spry PG, Scott SD (1986) The stability of zincian spinels in sulfide systems and their potential as exploration guides for metamorphosed massive sulfide deposits. Econ Geol 81:1446–1463

Toplis M, Corgne A (2002) An experimental study of element partitioning between magnetite, clinopyroxene and iron-bearing silicate liquids with particular emphasis on vanadium. Contrib Mineral Petrol 144:22–37

Walters SG, Skrzeczynski R, Whiting T, Bunting F, Arnold G (2002) Discovery and geology of the Cannington Ag-Pb-Zn deposit, Mount Isa Eastern Succession, Australia: development and application of an exploration model for Broken Hill-type deposits. Soc Econ Geol Spec Publ 9:95–118

Wang Q, Wu A, Yu L, Liu Z, Xu W, Yang H (2009) Nanocomposites of iron-cobalt alloy and magnetite: controllable solvothermal synthesis and their magnetic properties. J Phys Chem C 113:19875–19882

Williams PJ (1994) Iron mobility during synmetamorphic alteration in the Selwyn Range area, NW Queensland: implications for the origin of ironstone-hosted Au-Cu deposits. Miner Deposita 29:250–260

Williams PJ, Barton MD, Johnson DA, Fontboté L, de Haller A, Mark G, Oliver NHS, Marschik R (2005) Iron oxide copper-gold deposits: geology, space–time distribution, and possible modes of origin. Econ Geol 100th Anniversary Vol: 371–405